ISSN 214-453-2

EFFECT OF ANNEALING CONDITIONS ON THE MAGNETIC, OPTICAL AND PHOTOCATALYTIC PROPERTIES OF THE PEROVSKITE-TYPE MATERIAL $La_{1-x}(Bi_x)FeO_{3-\delta}$

IBRAHIM ABDULKADIR*[1], BICE S. MARTINCIGH[2] AND SREEKANTHA B. JONNALAGADDA[2]

[1]Department of Chemistry Ahmadu Bello University Samaru Zaria, Nigeria.

[2]School of Chemistry and Physics, University of KwaZulu-Natal, Westville Campus, Private Bag X54001, Durban 4000, South Africa

[Ibrahim.abdulkadir@gmail.com; +237 81 32 447776;]

ABSTRACT

Novel perovskite-type nanomaterials with the composition $La_{1-x}(Bi_x)FeO_{3-\delta}$ (where x = 0.5 and 0.2) were synthesized by using a modified citric acid sol-gel route and annealed at 900 °C in (1) in air (LB0.5FO-air and LB0.2FO-air), and (2) in Argon atmosphere (LB0.5FO-Ar and LB0.2FO-Ar). Scanning electron microscopy and powder X-ray diffraction analysis of the powders showed that they contain crystalline perovskite-type nanoparticles with crystallite sizes 37-41 nm. The lattice parameters, after refinement, showed that the particles crystallized in an orthorhombic structure. The BET specific surface areas (SSA) ranged between 1.76-4.37 $m^2 g^{-1}$ with powders synthesized under argon having the higher SSAs. Vibrating sample magnetometer analysis of the hysteresis loop showed a slightly higher magnetization value for the samples synthesized in air. Photoluminescence spectroscopy showed that the powders were all active in the visible region and could be useful for visible light photodegradation of organic dyes. The powders were all screened for photocatalytic activity against an organic dye (Rhodamine B) in the visible region of the solar spectrum and the photocatalytic activities were good for powders synthesized in argon, In addition, a mineralization of up to 80% was achieved after 3 hrs of photodegradation for these powders as well. The materials therefore, show good potential for the photocatalytic degradation of organic pollutants and photocatalyst recovery after photodegradation.

Keywords*: perovskites, magnetisation, photoluminescence, photocatalytic activities.*

Introduction

Perovskites are a group of materials that can generally be represented by the formula ABX_3 (where A^{3+} could be a large rare-earth metal, B^{3+} is a smaller transition metal and X^{2-} is a nonmetal, mostly, oxygen). The perovskite structure is flexible and can accommodate almost all the elements in the periodic table. Their tendency to display an array of very interesting properties have made them the focus of numerous scientific studies. Perovskites and perovskite-like multiferroic nanomaterials have potentials for application in a variety of crucial advanced technologies. They have been subjected to intensive investigation due to their potential for use as cathodes in solid oxide fuel cell (SOFC) (Skinner, 2001a, Skinner, 2001b, Maguire et al., 2000), sensors (Lantto et al., 2004, Ghasdi et al., 2011), piezo- and pyroelectric, acoustic transducers (Ramajo et al., 2014, Peel et al., 2013, Paik et al., 1999), capacitors and memory devises (Chung et al., 2008), as well as catalytic and photocatalytic materials (Zhu et al., 2014, Yu et al., 2012, Tang et al., 2007, Machida et al., 2000). For nanomaterials, the synthesis route have been shown to impact on the size and morphology as well as the surface area of the particles of the synthesized material and hence its properties. For perovskites and perovskite-like oxides, the annealing temperature for making the finished material is usually high and this leads to materials with large particle sizes and very low surface area, which is not good for photocatalysis (Zhu et al., 2014) for example, the optical and magnetic properties of these materials may also be affected. Annealing environment may also play a role in determining the properties of semiconductor oxides In this work, we prepare two sets of perovskite-like orthoferrites $La_{0.8}Bi_{0.2}FeO_3$ and $La_{0.5}Bi_{0.5}FeO_3$ via a modified sol gel method and proceed to anneal the powders under two different annealing conditions. First in air, and secondly under argon to determine how these annealing conditions could impact on the specific surface area, microstructural, magnetic, optical as well as photocatalytic properties of these materials.

Materials and Methods

Materials

$Fe(NO_3)_3.9H_2O$ (98 %), $Bi(NO_3)_3.5H_2O$ (97 %) (Saarchem), La_2O_3 (99.8 %), citric acid (BDH chemicals), chemically pure concentrated nitric acid, concentrated H_2SO_4 (98%), $HgSO_4$, ferrous ammonium sulfate (Merck), ethylene glycol (99%) (Promark Reagents) and H_2O_2 30% vol. (100 vol) (Minema Chemicals) were used as received. Deionised water from a Millipore Milli-Q Elix 5 UV system was used throughout this work.

Synthesis of $La_{(1-x)}Bi_xFeO_{3-\delta}$

$La_{(1-x)}Bi_xFeO_{3-\delta}$ (x = 0.5 for LB5FO, and 0.2 for LB2FO) samples were prepared by sol gel process. $Fe(NO_3)_3.9H_2O$ was dissolved in Milli Q water, La_2O_3 was dissolved in warm HNO_3 (about 15 cm^3, 5M) and $Bi(NO_3)_3.5H_2O$ in dilute nitric acid (about 10 cm^3 , 3M) solution to give the amount of metals required for both perovskites stoichiometries. The three solutions were

mixed thoroughly in each case, made up to 200 cm^3 and then gradually poured into a burette. The solutions were then mixed (dropwise) with a citric acid solution (400 cm^3, 0.15mols) in two separate beakers which are continuously being stirred by magnetic stirrers at room temperature to form clear solutions. Once the addition was completed for both solutions and still stirring, the temperature of the mixtures was raised to 90 ^oC and allowed to evaporate until the volume of the solution reduced to about 200 cm^3 in each case. 200 cm^3 of ethylene glycol was added to both solutions and the heating and stirring continued until a thick gel was formed in each beaker. The gel was then removed from the beakers and placed in crucibles in an oven at 120 ^oC for 24 hrs to dry the gels. The dry gels were subsequently pre-calcined at 400 ^oC for 4 hrs to remove all organic components and then a portion of the samples each were annealed at 900^oC in a muffle furnace (for LB2FO-air and LB5FO-air) and another portion of each powders was annealed under argon (to produce LB2FO-Ar and LB5FO-Ar) at same temperature for 4 hrs each.

Characterization and photocatalytic properties

Transmission electron microscopy (TEM) (JEOL JEM-1010) and high resolution transmission electron microscopy (HRTEM) (A JEOL-JEM 2100 LAB6) were used to analyze the shape and morphology of the crystals. Crystal structure and lattice parameter where determined by using powder X-ray diffraction (PXRD) analysis. The analysis was performed on a Bruker D8 advance diffractometer equipped with a Cu K_α radiation source (λ = 1.5406 Å). Crystallite sizes where determined by using the Scherrer equation $D = k\lambda/\beta\cos\theta$ (where D is the crystallite size, k is the Scherrer constant, λ is the wavelength of the radiation and β is the full width at half maximum). The surface area of each powder was determined with a Micromeritrics Tristar II surface area instrument by using nitrogen adsorption and the BET equation method. The magnetic properties were analysed with a Vibrating sample magnetometer (VSM) (LakeShore model 735) calibrated with a standard Ni sphere of saturation magnetization 54.7 emu g^{-1}, the maximum applied magnetic field was 14 kOe and all analyses were performed at room temperature. The thermal stability of the powders was determined using Themogravimetric analysis (TGA) measurements which were obtained for each sample in air using a TG/DTA thermal analyser (TA instruments SDT Q600 thermal analyzer). Fourier transform infrared (FTIR) spectroscopic data were recorded for each sample on a Perkin Elmer FTIR spectrum 100 fitted with an attenuated total reflectance (ATR) accessory.

Photocatalytic activities

The photocatalytic activity of the powders was tested on a model organic dye (rhodamine B (RhB) dye) in the presence of H_2O_2 at room temperature. The source of the white light was a 26 W fluorescent lamp (Osram Dulux D, 26 W, 1800 lm) placed in a quartz jacket at about 7 cm from the top of the dye solution. A fixed amount (1g dm^{-3}) of each of the powders was used for the test. The beaker containing the solution was placed on a magnetic stirrer and a 30 min period was allowed for equilibration to occur between the powder particles and the molecules of the dye solution. Aliquots of the irradiated dye solution were withdrawn at regular intervals and analyzed by means of a Biochrom Libra S6 UV spectrophotometer at the wavelength of maximum absorption (λ_{max}) for RhB (554 nm). Chemical oxygen demand (COD) analysis was used to study the mineralization of the dye solution by the photocatalyst after a photodegradation period of 180 min for each powder by using the standard procedure described in the literature (Williams, 2001). The % mineralization for each sample was calculated as follows $(COD_i - COD_f)/(COD)_i \times 100$.

Results and discussion

A fine brown powder was obtained after the precalcination process for each of the of the stoichiometries. The colour brightened up for samples annealed in air in a muffle furnace while the powders annealed under argon showed a dark brown colouration. All samples were collected in a sample vail, stored in a desiccators for further analyses.

Crystal lattices and cell parameters

The powder X-ray diffraction (PXRD) pattern of the samples indicate the presence of highly crystalline orthorhombic (space group Pnma) perovskite phases. Parameters obtained from the peak refinement using the EVA program on the DIFFRACT^{plus} evaluation package (2007) are displayed in Table 1. LB5FO shows the presence of a minute amount of impurity probably from phase separation due to the high annealing temperature (900 °C) used in this work. This phase separation could be as a result of the formation of a rhombohedral phase, likely, a $BiFeO_3$ phase indicated by the asteric (*) (Gonzalez Garcia et al., 2010). No other phase was observed on other diffractograms, which is an indication that all other ions have been well incorporated into the perovskite lattice. crystallite diameters calculated from the 110 peak broadening and Scherrer equation are quite close for both samples but the LB5FO have lager crystallites sizes of around 41 nm while the LB2FO have an average crystallite size of around 37 nm each (Table 1). The lattice cell parameter are also shown in Table 1. A general increase in the cell parameters of the powders is observed from powders with x = 0.5 to powders where x = 0.2. this is due to the larger size of La^{+3} ion substitute compared to the Bi^{+3} ion and it could also an indication that the La^{+3} ions have been incorporated into the perovskite crystal lattice. The cell parameters are, however, larger for the argon annealed samples and is an indication that annealing under argon conditions could allow for better replacement of the Bi^{+3} ions with the La^{+3} ions, and indeed this could be responsible for the appearance of the peak marked (*) on LB2FO-air and LB5FO-air (Fig. 1).

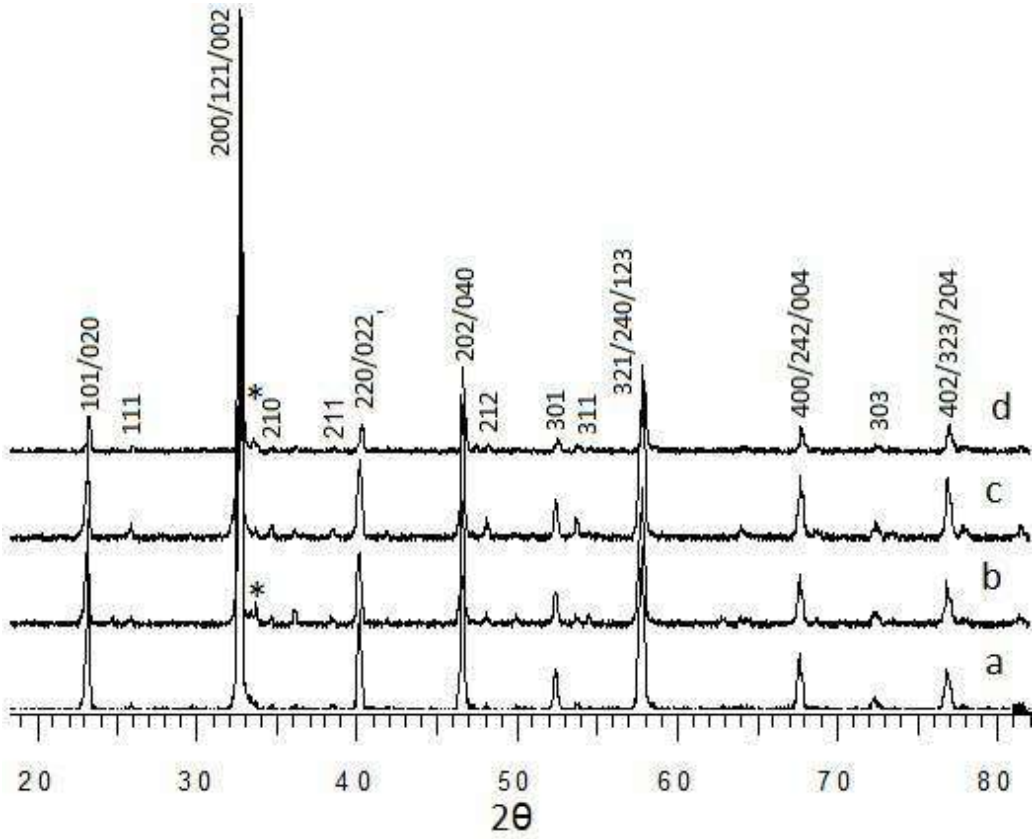

Figure 1: XRD peak pertterns showing orthorhombic (Pnma) peak perttern for (a) LB0.5FO-Ar, (b) LB0.5FO-air, (c) LB0.2FO-Ar and (d) LB0.2FO-air.

Table 1: Lattice parameter from peak refinement obtained from peak analysis from Diffrac^{Plus} software for LB5FO and LB2FO annealed under air and argon.

Sample	Lattice Parameter			Space group	Lattice system	Crystallite size (nm)
	A	B	C			
LB5FO-air	5.51363	7.82668	5.54305	Pnma	Orthorhombic	41.851
LB5FO-Ar	5.51260	7.82952	5.54392	Pnma	Orthorhombic	41.185
LB2FO-air	5.53402	7.85629	5.51557	Pnma	Orthorhombic	37.877
LB2FO-Ar	5.55182	7.85298	5.55018	Pnma	Orthorhombic	37.729

Microstructural characterization

TEM images shown in figure 2a, b, c. Confirm the crystal formation as observed from the PXRD peaks. The TEM images show spherical nanoparticles with size ranges between 35-50 nm in agreement with calculated average size ranges from Scherrer equation. Some spherical pores can also be seen on the LB5FO-Ar crystals (Fig. 2c). HRTEM (fig. 2d and e) presents lattice fringes for both powders showing regular d-spacing, which is an indication that LB5FO-air and LB2FO-air are well crystallized, similar results were obtained for LB2FO-Ar and to a lesser extent LB5FO-Ar. This explains the high peak intensities which were observed in the PXRD. The blurred appearance of the LB5FO-Ar however, is as a result of lattice defect and the presence of some pores on the crystals. The argon atmosphere leads to oxygen deficiency in the powder lattice which then results in the lattice defects as observed from the HRTEM images.

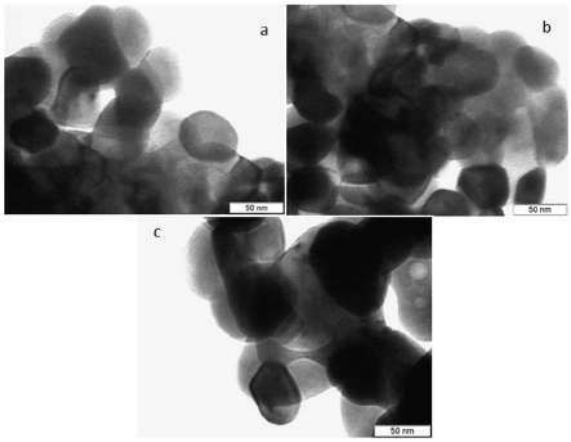

Figure 2(a-c): TEM images showing microstructure of powder crystals a) TEM image for LB5FO-air, b) TEM image for LB2FO-air, and c) TEM image for LB5FO-Ar.

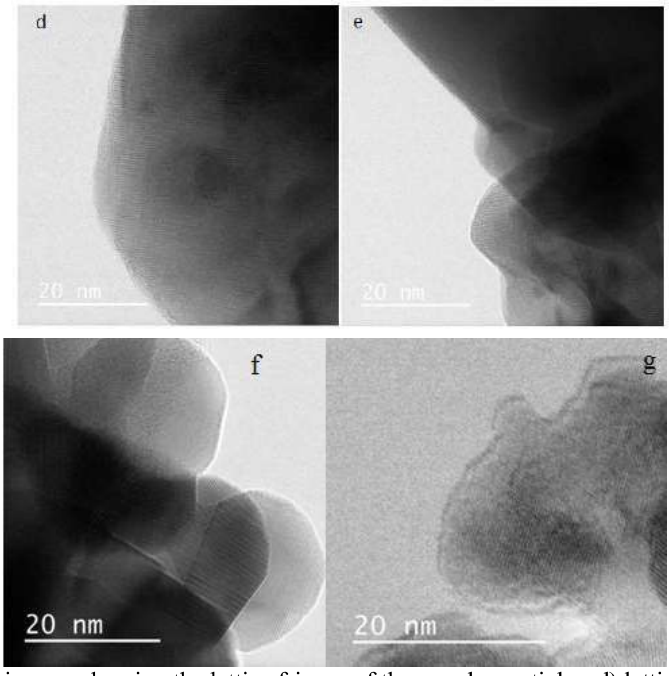

Figure 2 (d-g): HRTEM images showing the lattice fringes of the powder particles. d) lattice fringes for LB2FO-air, e) lattice fringes for LB5FO-air, f) lattice fringes for LB2FO-Ar and g) lattice fringes for LB5FO-Ar.

FTIR structure analyses

FT-IR-ATR spectra obtained for both powders are shown in figure 3. The only peaks observed are those at around 3500 to 3000 cm^{-1} and around 1460 cm^{-1} belonging to either the stretching or bending modes of water molecules and other OH^- groups adsorbed on the surface of the particles, Carbonyl peaks were not obsearved in both spectra. The most important peaks occur at around 380 and 550 cm^{-1} which represents the metal-oxygen stretching and oxygen-metal-oxygen bending modes of octahedradral MO_6 of perovskites (Parkin et al., 1996, Junploy et al., 2013, Jiang et al., 2011). Both spectra indicate that perovskiteO-Fe and O-Fe-O bonds have been produced in both cases. Similar results were obtained for LB2FO-air and LB2FO-Ar.

BET surface area

The specific surface area (SSA) values obtained for all the samples were generally low. The powders annealed under argon however, have relatively higher SSA values (Table 2). The low values obtained are due to the high annealing temperature used in this work. The nitrogen adsorption-desorption isotherms all conform to a type II IUPAC classification pattern (Fig. 4). There are no visible hysteresis on the isotherms for LB2FO-air, LB5FO-air and LB2FO-Ar, an indication of the absence of pores on the crystallites, the isotherm for LB5FO-Ar however, shows the presence of hysteresis, which indicates the presence of some mesopores on the LB5FO-Ar crystallites which is consistent with the TEM and HRTEM image results. The value of the P/P_0 (very close to1) also indicates that the mesopores are very few and would not impact drastically on the value of the SSA of the powder. The higher SSA values obtained for powders annealed under argon is connected to the oxygen deficiency which was created by the argon atmosphere, given rise to the lattice defects and formation of pores on the crystallites. This is also consistent with the SSA value of 7.85 m^2 g^{-1} obtained for LB5FO-Ar (Table 2). Overall, the SSA obtained for LB5FO-Ar is good for perovskites synthesized at similar annealing temperatures (BOUYSSIÉRES et al., 2005)

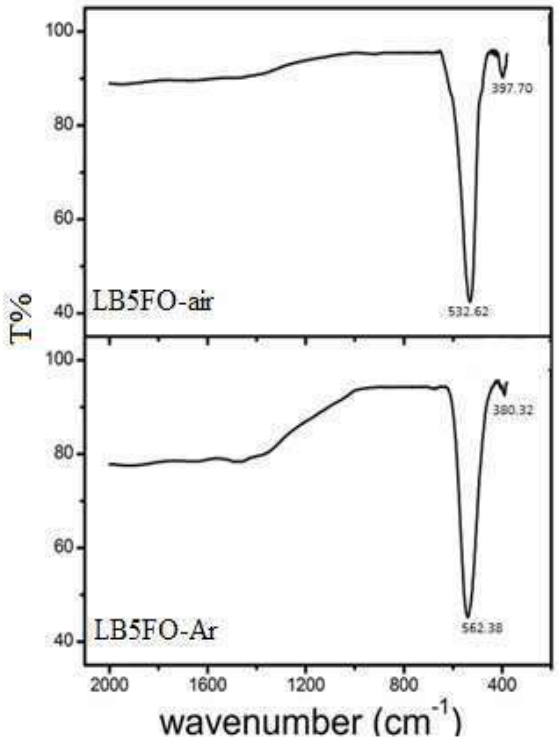

Figure 3: FTIR spectra for LB5FO-air and LB5FO-Ar, showing the stretching and bending modes for O-Fe and O-Fe-O of octahedral MO_6. Similar peaks were obtained for LB2FO-air and LB2FO-Ar.

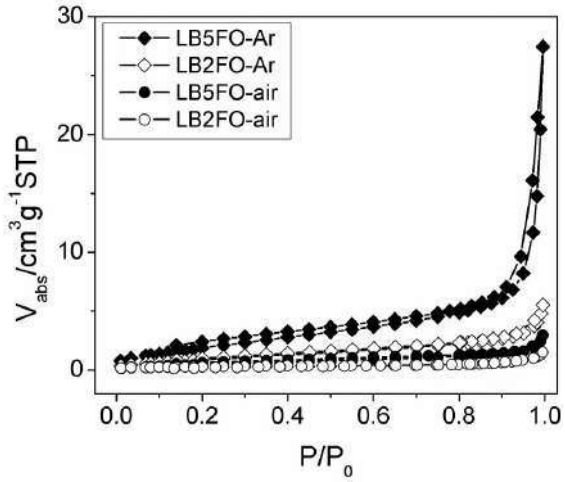

Figure 4: N_2 adsorption-desorption isotherms obtained at 77 K for LB2FO-air, LB5FO-air, LB2FO-Ar and LB5FO-Ar.

Magnetic properties

The M-H loops which shows the variation of magnetization relative to applied fields for both samples are shown in figure 5(a and b). The magnetization curve reveals a significant difference in the magnetic properties for powders annealed under air as compared to the magnetic properties of the powders annealed under argon at room temperature. The powders all showed weak ferromagnetic behavior and all the curves do not reach saturation. LB5FO-air shows a much higher magnetization relative to LB5FO-Ar and other powders, while the coercivity for LB5FO-Ar (H_C=206.12 Oe) is much larger than that for LB5FO-air which almost superparamagnetic with H_C =16.470 Oe. Table 2 shows the saturation magnetization M_S, remanant magnetization M_R, coercive field H_C, and squareness obtained from magnetization measurements for each powder. A magnification of the hysteresis (inset) reveals the coercive field and the exchange bias in both loops (Fig. 5b). perovskites have been shown to display a G-type weak ferromagnetism which arises due to spin canting in the perovskite lattice (Wang et al., 2009, Liang et al., 2005). The superparamagnetic nature of the LB5FO-air hysteresis might be due to the presence of a minute amount of a superparamagnetic secondary phase (e.g. γ-Fe_2O_3 or Fe_3O_4) which can enhance the magnetization of the powder.

Photoluminescence measurements

The room temperature photoluminescence (PL) activities in perovskites could arises due to the presence of some defects in the crystal lattice of the powder or as a result of the presence of oxygen vacancies which is referred to as the so-called intrinsic luminescence. The room temperature PL of the powders monitored at excitation wavelengths of 380, 390 and 400 nm are presented in Figure 6. All the powders showed a similar pattern of PL activity. Three narrow peaks were observed for the three different excitation wavelengths with a corresponding shift towards higher wavelengths. The highest peak intensity for the emission peaks occur at 590 nm corresponding to the 390 nm excitation wavelength for each powder. The excitation wavelengths used fall within the visible region of the electromagnetic spectrum and therefore is an indication that these powders could utilize visible light in order to degrade organic molecules. The residence time for the excited electron in LB5FO-Ar and LB5FO-air appear to be longer and this results in the low intensity observed in their emission peaks. This could also mean that these two powders would act as better visible light photocatalyst when compared to LB2FO-Ar and LB2FO-air. In all, this is an indication that perovskite PL is sensitive to annealing conditions.

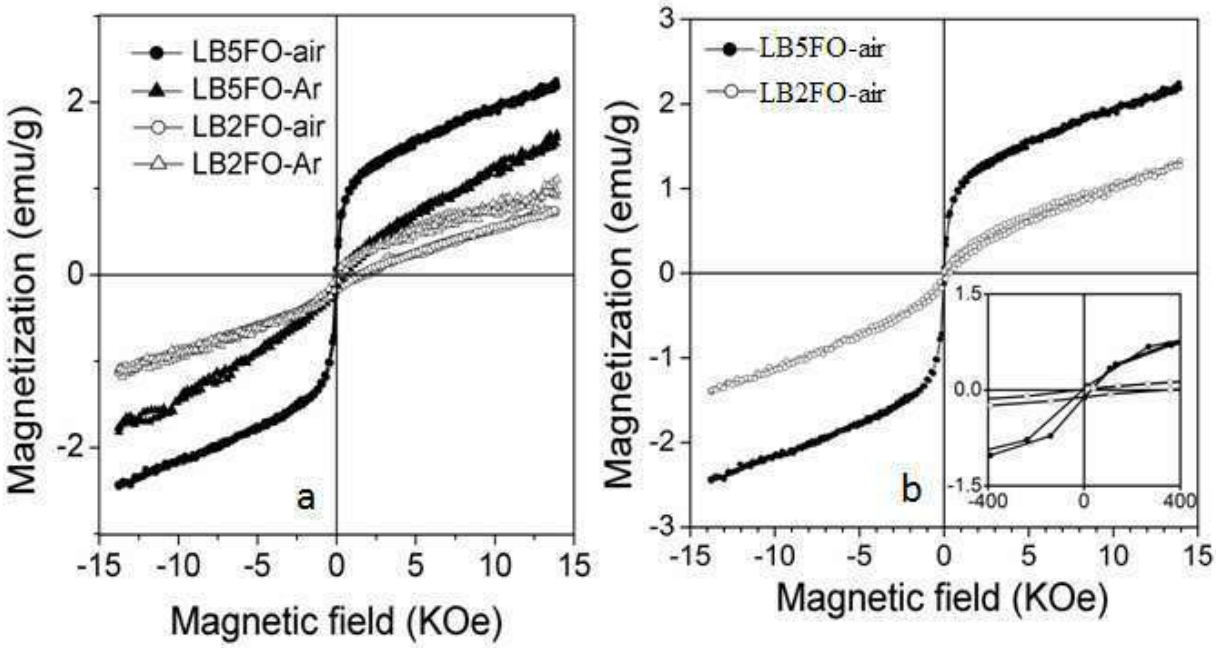

Figure 5: M-H Hysteresis loops a) for all four powders b) for LB5FO-air and LB5FO-Ar taken at room temperature.

Table 2: magnetization parameters obtained at room temperature for all the powder samples. SSA were obtained from N_2 adsorption-desorption at 77 K and the BET equation.

Sample	M_S (emu/g)	M_R (emu/g)	H_C (Oe)	M_S/M_R	SSA/m^2 g^{-1} (± 0.01)
LB5FO-air	2.2458	0.01827	16.470	0.02893	1.78
LB5FO-Ar	1.6555	0.03875	206.12	0.03944	7.85
LB2FO-air	1.1026	0.02743	174.64	0.05235	1.04
LB2FO-Ar	0.7535	0.14544	50.041	0.02386	3.29

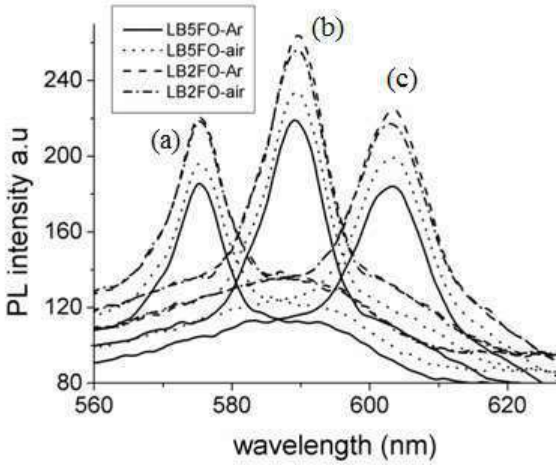

Figure 6: PL spectra showing a corresponding shift in the emission peak positions as excitation wavelength is shifted. These emission peaks correspond to excitation wavenumbers (a) λ_{ex} = 380 nm, (b) λ_{ex} = 390 nm and (c) λ_{ex} = 400 nm.

Photocatalytic screening

The photocatalytic screening of the materials (1g dm^{-3} of each powder) in the presence of H_2O_2 (100 µl) for photodegradation of the organic dye rhodamine B (RhB) is presented in Figure 7. Plots of A/A_0 against time show that the powders that have been annealed under argon are more active in the photodegradation of RhB (i.e. LB2FO-Ar>>LB2FO-air and LB5FO-Ar>>LB5FO-air). The ability of the argon annealed powders to be more active as photocatalyst may be as a result of the higher SSA as can beseen from the BET results or as a result of a more active surface than the powders that have been anneal in air, or a combination of both factors. The extent of mineralization after 180 min of photodegradation was obtained via a carbon oxygen demand (COD) analysis and the results of the analysis is shown in Figure 8. LB5FO-Ar and LB5FO-air recorded the highest values of % mineralization of 81 and 78% respectively (Table 3). Samples that have been annealed under argon show a better efficiency in photodegradation and mineralization of the RhB dye molecules.

Table 3: mineralization of RhB dye by synthesized powders after 180 min of photodegradation.

Sample	Mineralization (%)
LB2FO-air	51
LB2FO-Ar	53
LB5FO-air	78
LB5FO-Ar	81

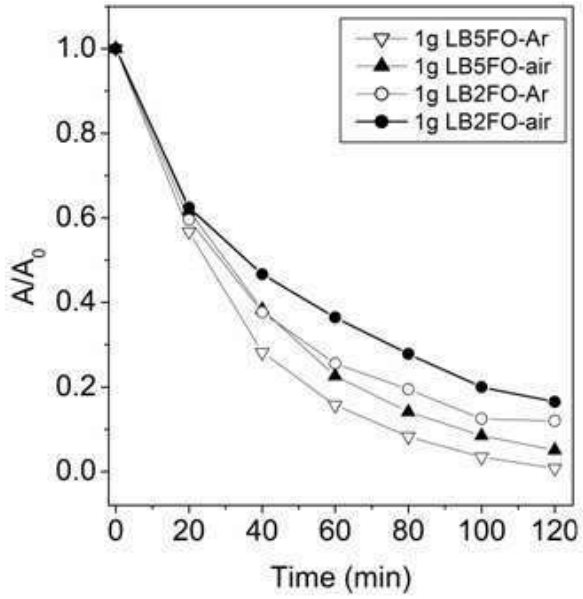

Figure 7: profile for photodegradation of RhB dye in the presence of H_2O_2. The activity of the powders is in the order LB5FO-Ar>LB5FO-air>LB2FO-AR>LB2FO-air.

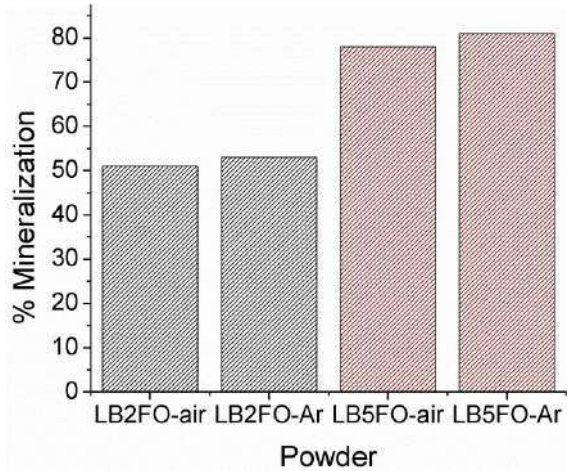

Figure 8: Analysis of the % mineralization for the synthesized powders after 180 min of photodegradation. Highest mineralization efficiency was obtained for LB5FO-Ar.

Conclusion

$La_{0.5}Bi_{0.5}FeO_3$ and $La_{0.8}Bi_{0.2}FeO_3$ have been synthesized and a portion annealed under air and another under argon. The PXRD analysis of the powders showed the formation of highly crystalline orthorhombic nanoparticles with size range between 37 and 42 nm.

TEM and HRTEM images also showed the formation of highly crystalline spherical nanoparticles whose size range in agrees with the calculated sizes from PXRD. The SSA were higher for powders annealed under argon. The VSM analysis of the magnetic properties of the powders showed a higher magnetisation for samples synthesized under air. The powders all showed active photoluminescence. Powders annealed under argon showed a higher photocatalytic efficiency in the degradation of RhB dye. In all, this work has shown that the annealing conditions under which perovskite materials are synthesized could influence the morphology as well as characteristics of the materials. In this work, annealing perovskites under argon appear to have improved the SSA of the materials as well as its ability to photodegrade the organic dye RhB. Photocatalyst recovery by the use of a magnet is also possible due to the weak ferromagnetism displayed by some of the powders.

References

BOUYSSIÉRES, L., SCHIFFERLI, R., URBINA, L., ARAYA, P. & PALACIOS, J. M. 2005. STUDY OF PEROVSKITES OBTAINED BY THE SOL-GEL METHOD. *Journal of the Chilean Chemical Society,* 50**,** 407-412.

CHUNG, C.-Y., CHANG, Y.-S., CHEN, G.-J., CHUNG, C.-C. & HUANG, T.-W. 2008. Effects of bismuth doping on the dielectric properties of Ba(Fe0.5Nb0.5)O3 ceramic. *Solid State Communications,* 145**,** 212-217.

GHASDI, M., ALAMDARI, H., ROYER, S. & ADNOT, A. 2011. Electrical and CO gas sensing properties of nanostructured $La_{1-x}Ce_xCoO_3$ perovskite prepared by activated reactive synthesis. *Sens. Actuat. B,* 156**,** 147-155.

GONZALEZ GARCIA, F., RICCARDI, C. S. & SIMÕES, A. Z. 2010. Lanthanum doped BiFeO3 powders: Syntheses and characterization. *Journal of Alloys and Compounds,* 501**,** 25-29.

JIANG, J., ZOU, J., ANJUM, M. N., YAN, J., HUANG, L., ZHANG, Y. & CHEN, J. 2011. Synthesis and characterization of wafer-like BiFeO< sub> 3</sub> with efficient catalytic activity. *Solid State Sciences,* 13**,** 1779-1785.

JUNPLOY, P., THONGTEM, S. & THONGTEM, T. 2013. Photoabsorption and photocatalysis of $SrSnO_3$ produced by a cyclic microwave radiation. *Superlattices and Microstructures,* 57**,** 1-10.

LANTTO, V., SAUKKO, S., TOAN, N. N., REYES, L. F. & GRANQVIST, C. G. 2004. Gas Sensing with Perovskite-like Oxides Having ABO_3 and BO_3 Structures. *Journal of electroceramics,* 13**,** 721-726.

LIANG, Y.-Q., DI, N.-L. & CHENG, Z.-H. 2005. Charge-disproportionation-induced magnetic glassy behavior in La0.5Ca0.5FeO3-δ. *Physical Review B,* 72**,** 134416.

MACHIDA, M., YABUNAKA, J.-I. & KIJIMA, T. 2000. Synthesis and Photocatalytic Property of Layered Perovskite Tantalates, RbLnTa2O7 (Ln = La, Pr, Nd, and Sm). *Chemistry of Materials,* 12**,** 812-817.

MAGUIRE, E., GHARBAGE, B., MARQUES, F. & LABRINCHA, J. 2000. Cathode materials for intermediate temperature SOFCs. *Solid State Ionics,* 127**,** 329-335.

PAIK, D. S., PARK, S. E., SHROUT, T. R. & HACKENBERGER, W. 1999. Dielectric and piezoelectric properties of perovskite materials at cryogenic temperatures. *Journal of Materials Science,* 34**,** 469-473.

PARKIN, I., KOMAROV, A. & FANG, Q. 1996. Alternative solid state routes to mixed metal oxides (LnCrO< sub> 3</sub>, LnFeO< sup> 3</sup>). *Polyhedron,* 15**,** 3117-3121.

PEEL, M. D., ASHBROOK, S. E. & LIGHTFOOT, P. 2013. Unusual Phase Behavior in the Piezoelectric Perovskite System, $Li_xNa_{1-x}NbO_3$. *Inorganic Chemistry,* 52**,** 8872-8880.

RAMAJO, L., CASTRO, M., DEL CAMPO, A., FERNANDEZ, J. & RUBIO-MARCOS, F. 2014. Influence of B-site compositional homogeneity on properties of $(K_{0.44}Na_{0.52}Li_{0.04})(Nb_{0.86}Ta_{0.10}Sb_{0.04})$ O_3-based piezoelectric ceramics. *Journal of the European Ceramic Society,* 34**,** 2249-2257.

SKINNER, S. J. 2001a. Recent advances in perovskite-type materials for SOFC cathodes. *Fuel Cells Bulletin,* 4**,** 6-12.

SKINNER, S. J. 2001b. Recent advances in Perovskite-type materials for solid oxide fuel cell cathodes. *International Journal of Inorganic Materials,* 3**,** 113-121.

TANG, J., ZOU, Z. & YE, J. 2007. Efficient Photocatalysis on BaBiO3 Driven by Visible Light. *The Journal of Physical Chemistry C,* 111**,** 12779-12785.

WANG, L., WANG, D., HUANG, H., HAN, Z., CAO, Q., GU, B. & DU, Y. 2009. The magnetic properties of polycrystalline $Bi_{(1-x)}$ Sr_xFeO_3 ceramics. *Journal of Alloys and Compounds,* 469**,** 1-3.

WILLIAMS, I. 2001. Environmental Chemistry; A Modular Approach. *Wiley.* 1 ed. UK: John Wiley & Son, Ltd.

YU, K., YANG, S., LIU, C., CHEN, H., LI, H., SUN, C. & BOYD, S. A. 2012. Degradation of Organic Dyes via Bismuth Silver Oxide Initiated Direct Oxidation Coupled with Sodium Bismuthate Based Visible Light Photocatalysis. *Environmental Science & Technology,* 46**,** 7318-7326.

ZHU, J., LI, H., ZHONG, L., XIAO, P., XU, X., YANG, X., ZHAO, Z. & LI, J. 2014. Perovskite Oxides: Preparation, Characterizations, and Applications in Heterogeneous Catalysis. *ACS Catalysis***,** 2917-2940.